The Astrophysical Journal, 841:22 (15pp), 2017 May 20 https://doi.org/10.3847/1538-4357/aa706d

The Evaporation and Survival of Cluster Galaxy Coronae. I. The Effectiveness of Isotropic Thermal Conduction Including Saturation

Rukmani Vijayaraghavan[1] and Craig Sarazin
Department of Astronomy, University of Virginia, 530 McCormick Rd., Charlottesville, VA 22904, USA; rukmani@virginia.edu
Received 2017 February 13; revised 2017 April 21; accepted 2017 April 27; published 2017 May 19

Abstract

We simulate the evolution of cluster galaxy hot interstellar medium (ISM) gas that is a result of the effects of ram pressure and thermal conduction in the intracluster medium (ICM). At the density and temperature of the ICM, the mean free paths of ICM electrons are comparable to the sizes of galaxies, therefore electrons can efficiently transport heat that is due to thermal conduction from the hot ICM to the cooler ISM. Galaxies consisting of dark matter halos and hot gas coronae are embedded in an ICM-like "wind tunnel" in our simulations. In this paper, we assume that thermal conduction is isotropic and include the effects of saturation. We find that as heat is transferred from the ICM to the ISM, the cooler denser ISM expands and evaporates. This process is significantly faster than gas loss due to ram pressure stripping; for our standard model galaxy, the evaporation time is 160 Myr, while the ram pressure stripping timescale is 2.5 Gyr. Thermal conduction also suppresses the formation of shear instabilities, and there are no stripped ISM tails since the ISM evaporates before tails can form. Observations of long-lived X-ray emitting coronae and ram pressure stripped X-ray tails in galaxies in group and cluster environments therefore require that thermal conduction is suppressed or offset by some additional physical process. The most likely process is anisotropic thermal conduction that is due to magnetic fields in the ISM and ICM, which we simulate and study in the next paper in this series.

Key words: conduction – galaxies: clusters: intracluster medium – galaxies: clusters: general – galaxies: evolution – shock waves

1. Introduction

Galaxies in cluster environments are gas poor (e.g., Davies & Lewis 1973; Haynes & Giovanelli 1984; Solanes et al. 2001; Boselli & Gavazzi 2006; Cortese et al. 2011; Jaffé et al. 2016), and consequently, they have on average significantly lower star formation rates and higher early type fractions than galaxies in the field (Dressler 1980; Kennicutt 1983; Postman & Geller 1984; Zabludoff & Mulchaey 1998; Lewis et al. 2002; Gómez et al. 2003; Weinmann et al. 2006; Rasmussen et al. 2012; Haines et al. 2013). In these dense environments with deep potential wells, galaxies are stripped of dark matter, stars, and gas through tidal forces and harassment (Moore et al. 1996, 1998; Gnedin 2003a, 2003b; Mastropietro et al. 2005; Villalobos et al. 2012, 2014). The hot X-ray emitting intracluster medium (ICM), with temperatures $T_{\rm ICM} \sim 10^7$–10^8 K and densities $n_{\rm e} \sim 10^{-3}$ cm^{-3}, exerts ram pressure on the interstellar medium (ISM) gas in galaxies (Gunn & Gott 1972; Quilis et al. 2000). Ram pressure causes a drag force that may remove the hot coronal/halo component of the ISM (Larson et al. 1980; Kawata & Mulchaey 2008; McCarthy et al. 2008; Shin & Ruszkowski 2014; Roediger et al. 2015a, 2015b), as well as the cold molecular and atomic ISM (Schulz & Struck 2001; Vollmer et al. 2001; Roediger et al. 2006; Kapferer et al. 2009; Tonnesen & Bryan 2009; Ruszkowski et al. 2014; Tonnesen & Stone 2014). In addition, thermal conduction can transfer heat from the ICM to the ISM, resulting in the evaporation of the hot ISM (Cowie & Songaila 1977; Sarazin 1986).

On the other hand, X-ray observations of cluster galaxies reveal that a significant fraction of cluster galaxies have compact X-ray emitting coronae. Vikhlinin et al. (2001) observed the two central galaxies in the Coma cluster with *Chandra* and detected compact (∼3 kpc) X-ray coronae of 1–2 keV centered on these galaxies. These coronae were studied in more detail by Sanders et al. (2014). Later studies extended these observations to other central (Yamasaki et al. 2002) and satellite galaxies in clusters (e.g., Sun et al. 2005a, 2005b). Systematic studies by Sun et al. (2007) showed that ∼60% of $L_K > 2L_*$ galaxies in rich clusters have compact X-ray emitting coronae. Jeltema et al. (2008) showed that an even larger fraction of group galaxies have X-ray coronae, up to 80% of $L_K > L_*$ galaxies. The frequency of these detections in group and cluster galaxies implies that galactic coronae survive for timescales on the order of many orbital times in clusters. These observations contradict theoretical expectations for gas retention timescales in cluster galaxies that are subject to ram pressure stripping and evaporation that is due to thermal conduction.

The rate at which a galaxy is stripped of its gas by ram pressure ($P_{\rm ram} = \rho_{\rm ICM} v_{\rm galaxy}^2$) is determined by the galaxy orbit within the cluster, including the orbital ellipticity, the pericentric distance to the cluster center, which affects both the local $\rho_{\rm ICM}$ encountered by the galaxy and the maximum orbital velocity, and the average orbital velocity of the galaxy. The galaxy resistance to ram pressure is driven by its internal thermal pressure, which, assuming hydrostatic equilibrium, is determined by its density profile and gravitational potential; one expects that more massive galaxies are more strongly resistant to ram pressure. Using simulations of a cluster with a realistic population of initially hot ISM gas-rich galaxies, Vijayaraghavan & Ricker (2015) showed that even relatively massive galaxies ($M > 10^{11}\,M_\odot$) lose 90% of their gas mass within 2.5 Gyr over a range of galaxy orbits and velocities; lower mass galaxies lose all their gas within this period. Massive galaxies lose all of their gas within 4–5 Gyr. These

[1] NSF Astronomy & Astrophysics Postdoctoral Fellow.

timescales are an upper limit for the removal of the hot coronal ISM, since in these simulations the coronae/hot halos in galaxies extend out to the galaxies' virial radius and comprise 10% of the galaxies' mass. Ram pressure alone can therefore efficiently remove the hot coronal gas within one dynamical time ($t_{\rm dynamical} \sim$ 2–3 Gyr for rich clusters).

Thermal conduction, that is, the transfer of heat via electrons and ions, affects the evolution of the ICM in various ways. The transfer of heat from the hotter outer ICM to the cooler core, which suppresses cooling and thereby subsequent star formation, has been proposed as a partial solution to the cooling flow problem in clusters (e.g., Bertschinger & Meiksin 1986; Narayan & Medvedev 2001; Zakamska & Narayan 2003; Ghizzardi et al. 2004; Jubelgas et al. 2004; Voigt & Fabian 2004; Wagh et al. 2014). A caveat with this process is that thermal conduction can be suppressed by ICM magnetic fields to values significantly below the classical Spitzer value (Spitzer 1962). We explore the particular effects of anisotropic thermal conduction that is due to magnetic fields on galactic coronae in the next paper in this series (Paper II). Thermal conduction has also been proposed as a potential mechanism to transport heat generated by a central AGN to the outer regions of clusters (reviewed in McNamara & Nulsen 2007). Using numerical simulations, Dolag et al. (2004) showed that thermal conduction can result in an isothermal ICM core, but is less effective in cool core clusters. Smith et al. (2013) also studied the effect of isotropic thermal conduction on ICM temperature profiles, finding that including conduction resulted in more isothermal cores and a thermally uniform ICM. Voit (2011) suggested that radiatively cooled gas in cluster cores can trigger AGN feedback when thermal conduction cannot balance cooling.

At typical temperatures of the ICM and galactic coronae, thermal conduction can be particularly effective in transporting heat from the ICM to ISM. The mean free path of ICM electrons is ∼10 kpc, which is comparable to the sizes of galactic coronae. When isotropic thermal conduction is assumed, ICM electrons can transport heat between the ISM and ICM (Spitzer & Härm 1953; Sarazin 1986). The expected timescale for this process assuming steady-state evaporation and mass loss for a uniform constant density ($\bar{n}$) sphere of radius R (in kpc) is $t_{\rm evap} = 3.3 \times 10^{20} \bar{n} R^2 T^{-5/2} (\ln\Lambda/30)$ Myr (Cowie & McKee 1977). $t_{\rm evap} \sim 10^7$ years for the parameters of a typical galaxy, which is significantly shorter than the ram pressure stripping timescale of $\sim 3 \times 10^9$ years, although this assumption does not include the effects of a gravitational potential and a density and temperature gradient. Cowie & Songaila (1977) also calculated the evaporation timescales of galaxies embedded in 10^8 K gas; their calculated timescale is proportional to the size of coronae, but is significantly shorter than ram pressure stripping times and mass loss replenishment from stars. A combination of thermal conduction, which evaporates the ISM and results in a more uniform temperature distribution, ram pressure stripping, which removes any remnant ISM gas, and tidal stripping, which decreases the depth of the galaxies' potential well, should therefore efficiently remove hot galactic coronae.

Gas removal from cluster galaxies must therefore be offset by physical mechanisms that shield against stripping and conduction or replenish gas loss from galaxies. The ICM is threaded by μG magnetic fields (e.g., as reviewed in Carilli & Taylor 2002; Govoni & Feretti 2004; Kronberg 2005; Ryu et al. 2012), which can suppress shear instabilities that are precursors to the dissipation of the ISM at the the ISM-ICM interface. However, the magnetic pressure in the ICM is $\sim 10^2$ times weaker than the thermal and ram pressure and therefore does not quantitatively affect the hydrodynamics of the stripping processes (Ruszkowski et al. 2014; Shin & Ruszkowski 2014; Tonnesen & Stone 2014; Vijayaraghavan & Ricker 2017). On the other hand, magnetic fields will affect the rate of ISM evaporation that is due to thermal conduction. In the presence of a local magnetic field, electrons will gyrate around the magnetic field (Spitzer 1962). The gyroradius of a typical electron ($r_g = m v_\perp c/qB$) is $\sim 2 \times 10^8$ cm, which is significantly smaller than electron mean free paths. Electrons therefore cannot cross magnetic field lines and are constrained to only transport heat along the direction of the magnetic field. This anisotropic thermal conduction can drastically reduce the effectiveness of evaporation that is due to thermal conduction. A viscous ICM will also suppress shear instabilities (Roediger et al. 2013b, 2015b). Magnetic fields and viscosity therefore qualitatively affect the stripping of galaxies, which results in more coherent, long-lived stripped tails, but they do not dramatically affect the gas loss rate of galactic coronae through stripping.

In this paper (Part I) and in the following paper on anisotropic thermal conduction in cluster galaxies, we simulate galaxies embedded in wind tunnel simulation boxes with ICM-like physical properties. In Part I we describe the process of gas loss from isotropic thermal conduction including saturation, in the absence of magnetic fields. We quantify the gas loss rate of galaxies from thermal conduction and ram pressure stripping, the evolution of the effective heat flux as the galaxy evaporates, and the effectiveness of thermal conduction on varying galaxy mass and ICM densities. In Part II we describe the effect of magnetic fields and the subsequent anisotropic thermal conduction on stripping and evaporation over a range of magnetic field configurations that either shield the galaxy or connect the galaxy and the ICM, the longevity of stripped tails, the relationship between tail morphology and magnetic field configuration, and the timescale over which gas evaporates as a result of anisotropic thermal conduction.

2. Simulation Methods

We use the FLASH 4.3 code (Fryxell et al. 2000; Dubey et al. 2008), a parallel N-body plus Eulerian hydrodynamics code with adaptive mesh refinement (AMR), to perform the simulations in this paper. Our simulations consist of galaxies with dark matter and gas components in a wind tunnel of ICM gas. In our simulations, massive particles are mapped to the grid using cloud-in-cell mapping. The potential on the mesh is calculated from the total dark matter plus gas density using the direct multigrid solver (Ricker 2008). AMR is implemented on the Eulerian mesh in FLASH using PARAMESH (MacNeice et al. 2000). We use the directionally split piecewise-parabolic method solver in FLASH to evolve Euler's equations of hydrodynamics. Thermal conduction is explicitly implemented by calculating the heat flux on the boundaries of each cell, as described below, and the subsequent change in internal energy for a given cell. The computational timestep is diffusion limited to ensure stability.[2]

[2] $\Delta t = 0.5 \frac{\Delta x^2}{D}$, with $D = \kappa/\rho c_v$, where κ is the conductivity, ρ is the gas density, and c_v is the specific heat capacity.

2.1. Theoretical Background: Evaporation of Coronae in a Hot ICM

Cool galactic coronae embedded in hot intracluster media form temperature gradients. In the absence of magnetic fields and any other heat sources, the temperature gradient will result in the flow of heat, primarily through electrons, from the hot ICM to the cooler galactic ISM (Spitzer & Härm 1953; Spitzer 1962). As a result, the galactic ISM gas will expand and evaporate into the ICM. Quantitatively, the flow of heat is expressed in the form of the heat flux, $\boldsymbol{Q}$, where

$$\boldsymbol{Q} = -\kappa \boldsymbol{\nabla} T_{\rm e}, \tag{1}$$

with

$$\kappa = \epsilon \delta_T \kappa_{\rm Sp}, \tag{2}$$

where $\boldsymbol{\nabla} T_{\rm e}$ is the temperature gradient, κ is the conduction coefficient, and $\epsilon = 0.419$ and $\delta_T = 0.225$ for a hydrogen ($Z = 1$) plasma. $\kappa_{\rm Sp}$, the Spitzer thermal conductivity, is

$$\kappa_{\rm Sp} = 20\left(\frac{2}{\pi}\right)^{3/2} \frac{k_{\rm B}^{7/2} T_{\rm e}^{5/2}}{m_{\rm e}^{1/2} q_{\rm e}^4 Z \ln\Lambda}. \tag{3}$$

Here, $k_{\rm B}$ is the Boltzmann constant, $T_{\rm e}$ is the electron temperature, $m_{\rm e}$ and $q_{\rm e}$ are the mass and charge of an electron, and $\ln \Lambda$ is the Coulomb logarithm,

$$\ln \Lambda = 37.8 + \ln\left[\left(\frac{T_{\rm e}}{10^8\ {\rm K}}\right)\left(\frac{n_{\rm e}}{10^{-3}\ {\rm cm}^{-3}}\right)\right]. \tag{4}$$

Thermal conduction in these media is primarily carried out through electrons, since $\kappa_{\rm Sp} \propto m_{\rm e}^{-1/2}$. The electron mean free path is (Spitzer 1962; Sarazin 1986)

$$\lambda_{\rm e} = \frac{3^{3/2}(k_{\rm B} T_{\rm e})^2}{4\pi^{1/2} n_{\rm e} q_{\rm e}^4 \ln\Lambda} \simeq 22\ {\rm kpc}\left(\frac{T_{\rm e}}{10^8\ {\rm K}}\right)^2\left(\frac{n_{\rm e}}{10^{-3}\ {\rm cm}^{-3}}\right)^{-1}. \tag{5}$$

The Spitzer thermal conductivity can therefore be written as

$$\kappa_{\rm Sp} = 13.8\, n_{\rm e} \lambda_{\rm e} \frac{k_{\rm B}^{3/2} T_{\rm e}^{1/2}}{m_{\rm e}^{1/2}}\ {\rm erg\ cm^{-1}\ s^{-1}\ K^{-1}}. \tag{6}$$

The heat flux, $\boldsymbol{Q}$, is inversely proportional to the length scale of the temperature gradient, l_T; the lower the value of l_T, the higher the heat flux. However, Cowie & McKee (1977) show that since the rate at which heat is transported is limited by the average electron speed in a given medium, the effective heat flux can saturate. They find that the magnitude of the saturated heat flux when $\lambda_{\rm e} \gg l_T$ is

$$Q_{\rm sat} = 0.4\left(\frac{2 k_{\rm B} T_{\rm e}}{\pi m_{\rm e}}\right)^{1/2} n_{\rm e} k_{\rm B} T_{\rm e}. \tag{7}$$

The effective heat flux is obtained by interpolating between $\boldsymbol{Q}$ and $\boldsymbol{Q}_{\rm sat}$:

$$\frac{1}{\boldsymbol{Q}_{\rm eff}} = \frac{1}{\boldsymbol{Q}} + \frac{1}{\boldsymbol{Q}_{\rm sat}}. \tag{8}$$

In terms of the heat flux ratio, $\sigma = Q/Q_{\rm sat}$, the effective heat flux is

$$\boldsymbol{Q}_{\rm eff} = \frac{-\kappa \boldsymbol{\nabla} T_{\rm e}}{1 + \sigma}, \tag{9}$$

which alternatively reduces to

$$\boldsymbol{Q}_{\rm eff} = \frac{\kappa T_{\rm e}}{l_T + 4.2\lambda_{\rm e}} \frac{\boldsymbol{\nabla} T_{\rm e}}{|\boldsymbol{\nabla} T_{\rm e}|}. \tag{10}$$

When $l_T \gg \lambda_{\rm e}$, the effective heat flux obeys the classical form, while in the regime of $l_T \ll \lambda_{\rm e}$, the effective heat flux is saturated. For typical galactic coronae in cluster environments, $l_T \simeq \lambda_{\rm e}$ since the sizes of typical galactic coronae are comparable to the electron mean free paths in Equation (5). Thermal conduction in these regions is therefore at least partially saturated.

2.2. Initial Conditions

We perform a series of "wind tunnel" simulations of a galaxy embedded in an ICM-like wind. These simulations, in the rest frame of the galaxy, consist of a galaxy in the center of a cubic box. One side of the box is an inflow boundary through which the ICM gas flows in at a constant velocity. The other five sides of the box are outflow boundaries. The density, pressure, and temperature of the ICM wind are initially constant throughout the box. The center of the galaxy is at the center of the box, to prevent the development of an artificial potential gradient within the box from an asymmetric mass distribution of the ICM wind with respect to the galaxy.

The galaxy consists of a spherically symmetric dark matter potential and hot ISM gas in hydrostatic equilibrium with the gravitational potential. The galaxy's dark matter component and gas are initialized using the procedure described in Vijayaraghavan & Ricker (2015), which we summarize here. The galaxy's total density profile is

$$\rho_{\rm tot} = \rho_{\rm DM} + \rho_{\rm ISM} + \rho_{\rm ICM,background}. \tag{11}$$

This total density profile is described by a Navarro-Frenk-White (Navarro et al. 1997) profile,

$$\rho_{\rm tot}(r \leqslant R_{200}) = \frac{\rho_{\rm s}}{r/r_{\rm s}(1 + r/r_{\rm s})^2}, \tag{12}$$

where R_{200} is the galaxy's virial radius, and $r_{\rm s}$ and $\rho_{\rm s}$ are the scale radius and scale density parameters. $\rho_{\rm ICM,background}$ is the gas density beyond the ISM and is initially constant, while $\rho_{\rm ISM}$ is assumed to be a singular isothermal sphere distribution with

$$\rho_{\rm ISM}(r \leqslant R_{200}) = \frac{\rho_0 r_0^2}{r^2}. \tag{13}$$

We assume that the gas mass fraction of the ISM is 10% of the total mass of the galaxy, not including the background ICM. At $r > R_{200}$, the dark matter is assumed to have an exponential fall off in density, and the density of gas is the constant ICM background density. Given the dark matter density profile, $\rho_{\rm DM} = \rho_{\rm tot} - \rho_{\rm ISM} - \rho_{\rm ICM,background}$, we initialize the positions and velocities of massive dark matter particles to determine the galaxy's gravitational potential as described in Vijayaraghavan & Ricker (2015), using the procedure outlined in Kazantzidis et al. (2004).

The galaxy's pressure profile is initialized assuming hydrostatic equilibrium, where $\rho_{\rm gas} = \rho_{\rm ISM} + \rho_{\rm ICM,background}$ and Φ is the total gravitational potential,

$$\frac{dP}{dr} = -\rho_{\rm gas} \frac{d\Phi}{dr}. \tag{14}$$

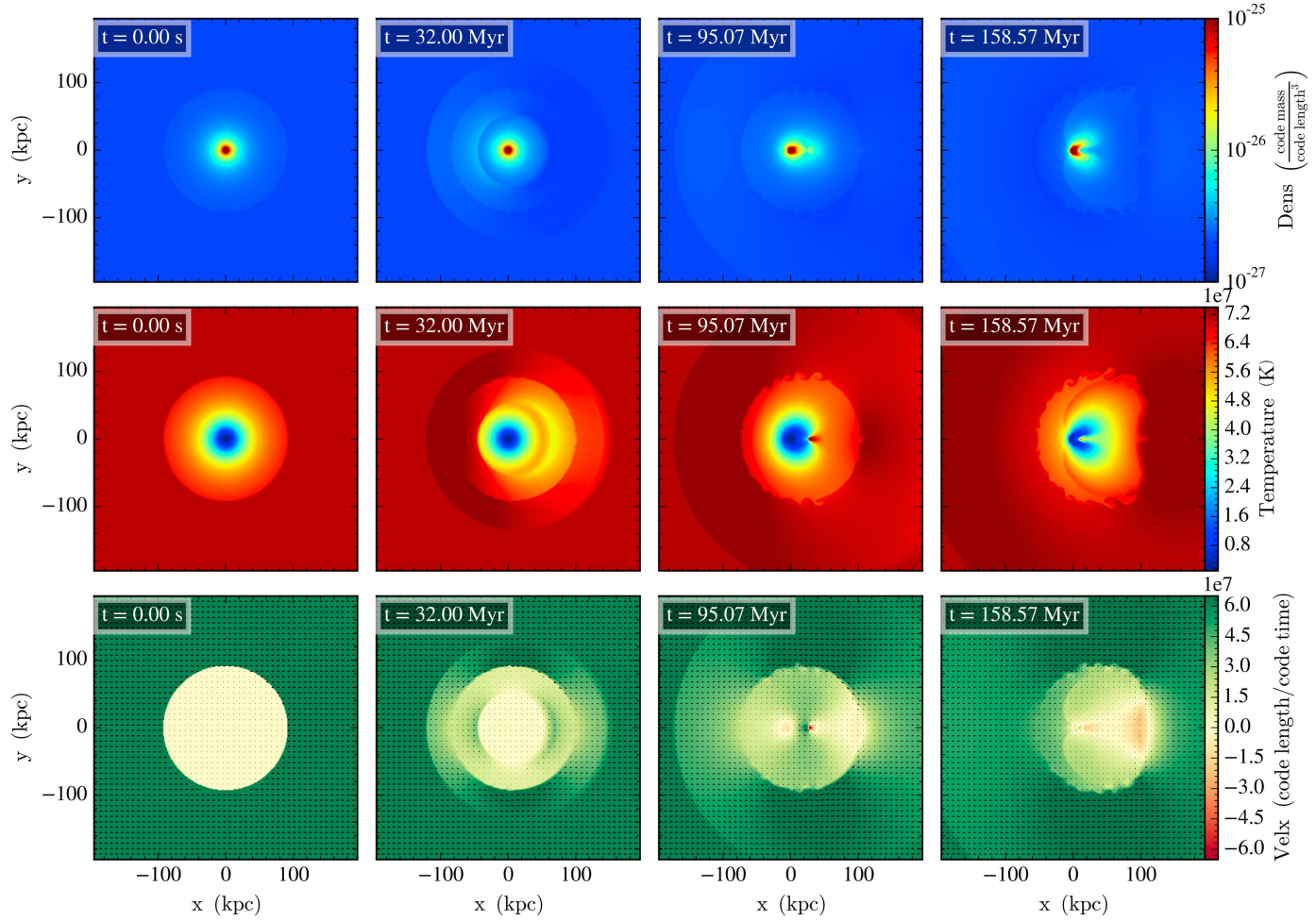

Figure 1. Slices of density, temperature, and the x component of the velocity in a simulation of gas loss from ram pressure with no thermal conduction from $t = 0$–160 Myr. The velocity slices are annotated with velocity vectors.

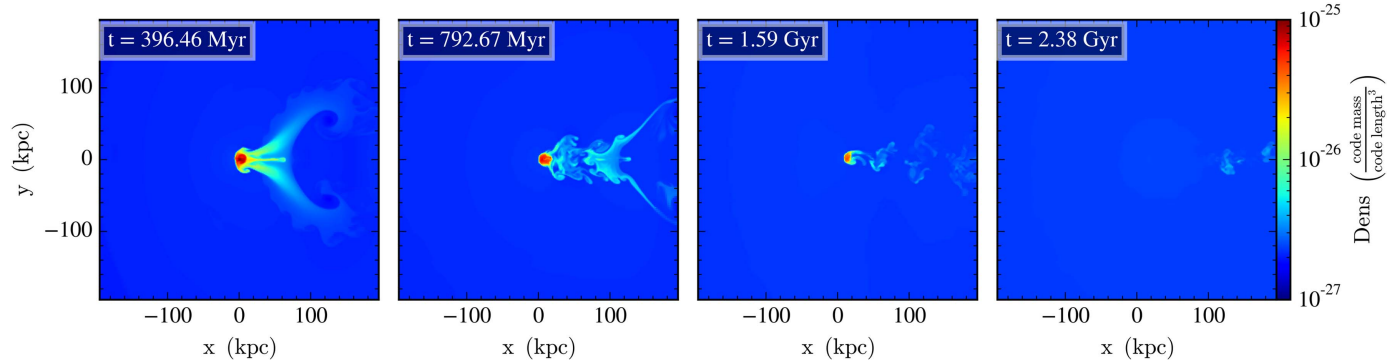

Figure 2. Slices of density in a simulation of gas loss from ram pressure with no thermal conduction from $t = 400$–2400 Myr.

The temperature T is calculated from the usual ideal gas law,

$$P = \frac{k_{\rm B}}{\mu m_{\rm p}} \rho_{\rm gas} T, \tag{15}$$

where $k_{\rm B}$ is the Boltzmann constant, $\mu \simeq 0.59$ is the mean molecular weight for a fully ionized hydrogen-helium plasma, and $m_{\rm p}$ is the proton mass. We assume a constant $\gamma = 5/3$ equation of state throughout. The density, temperature, and pressure of the galaxy are continuous with the background ICM at $r = R_{200}$. In our base series of simulations, we adopt $\rho_{\rm ICM} = 2 \times 10^{-27}$ g cm^{-3}, $P_{\rm ICM} = 2 \times 10^{-11}$ erg cm^{-3}, and $T_{\rm ICM} = 7.14 \times 10^7$ K. The mass of the galaxy is $M_{200} = 2.8 \times 10^{11}\, M_\odot$, its virial radius is $R_{200} = 92.16$ kpc, and its scale radius is $R_{\rm s} = 18.43$ kpc. We also ran a simulation with a lower density ICM, with $\rho_{\rm ICM} = 2 \times 10^{-28}$ g cm^{-3}, $P_{\rm ICM} = 2 \times 10^{-12}$ erg cm^{-3}, and $T_{\rm ICM} = 7.14 \times 10^7$ K, and of a higher mass galaxy with $M_{200} = 2.8 \times 10^{12}\, M_\odot$ with a virial radius of $R_{200} = 190$ kpc. The galaxy properties for both the standard galaxy and the higher

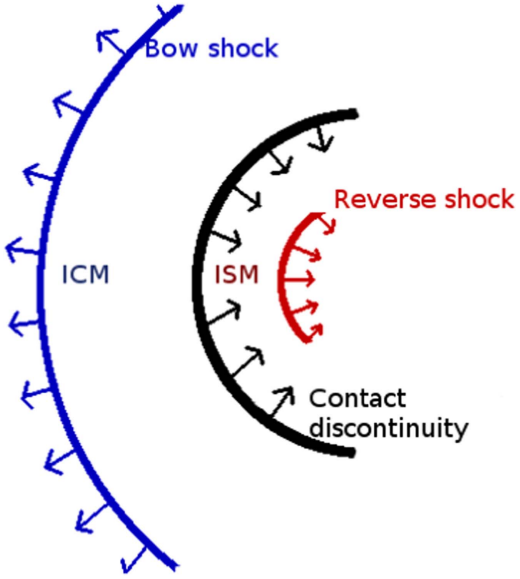

Figure 3. Sketch illustrating the relative positions and directions of propagation of the bow shock, contact discontinuity at the ICM–ISM interface, and reverse shock.

mass case were chosen from the galaxy sample in Vijayaraghavan & Ricker (2015), where these properties are discussed further. We note that the galaxy scale radius and gas density profile slope do not have a significant effect on ram pressure stripping (Vijayaraghavan & Ricker 2015).

3. Results

3.1. No Evaporation, with Ram Pressure

In this section, we discuss the stripping of a galaxy's hot ISM gas as a result of ram pressure. We performed a base simulation run of the model galaxy in an ICM wind tunnel without thermal conduction. Under these simulated conditions, ram pressure that is due to the ICM wind is the only physical process by which the galaxy can lose its gas. At $t = 0$ Myr, the density, temperature, and pressure of the ICM and ISM are continuous at the galaxy's virial radius, R_{200}. The galaxy and the ISM are at rest in the frame of the simulation box. The simulation box is three-dimensional and cubic, with each side of length 2×10^{24} cm, or 648 kpc. The ICM wind flows into the box through the $-\boldsymbol{x}$ face. The other five faces of the box have outflow boundaries. The ICM wind has a velocity $\boldsymbol{v}_{\rm ICM} = v_{\rm ICM}\hat{x}$, with $v_{\rm ICM} = 610\,{\rm km\,s^{-1}}$.

In more massive clusters, galaxy velocities can be higher, $\gtrsim 10^3\,{\rm km\,s^{-1}}$. Since the ram pressure is $P_{\rm ram} \propto \boldsymbol{v}_{\rm ICM}^2$, at higher velocities and therefore in massive clusters, galaxies will be stripped of their gas at a faster rate (shown in Vijayaraghavan & Ricker 2015). Additionally, in realistic cluster environments, galaxy orbital velocities will vary considerably unless they are on circular orbits, which results in a range of ram pressure values encountered by galaxies. However, most of the galaxies' gas loss occurs during their first orbit within their host cluster ($t \sim$ 2–3 Gyr), when the galaxies' outer halos are stripped rapidly until their internal thermal pressure balances the sum of the ICM thermal pressure and ram pressure (Vijayaraghavan & Ricker 2015), followed by a slower disruption of the core. Therefore, the timescale for gas loss is determined by both the maximum ram pressure experienced by the galaxies and when galaxies encounter this ram pressure.

Figure 1 shows slices of the ISM and ICM density, temperature, and x component of the velocity in the $z = 0$ plane. Figure 2 shows density slices at later times. There is an initial contact discontinuity at the galaxy virial radius on the side facing the incoming ICM wind. At this interface, as the ICM flows past the galaxy, shear instabilities leading to Kelvin-Helmholtz (KH) rolls are formed. A bow shock propagates out from the leading surface of the galaxy into the ICM (illustrated in Figure 3). A reverse shock propagates inward to the center of the galaxy and penetrates the core of the galaxy at $t = 72$ Myr. The reverse shock is refracted around the core and converges behind the core (at $t =$ 88–95 Myr). The density and pressure within the core drop significantly after the reverse shock has passed through the core ($t =$ 100–120 Myr). Gas flows into the core to maintain hydrostatic equilibrium, and a second shock then propagates outward from where the initial reverse shock converged, through the core. As this shock passes through the core, the core gas is compressed, resulting in increased core density and pressure. This compression delays the stripping of the core. The second shock propagates behind the initial bow shock; there is no subsequent reverse shock. The force due to ICM ram pressure pushes on the outer diffuse ISM and strips it away. The stripped ISM gas trails the galaxy initially in a hollow cylindrical tail.

After the lower density, outer ISM gas is stripped, the denser core ISM gas is stripped away at a much slower rate (from $t \simeq 300$ Myr to $t \simeq 1600$ Myr) and trails the galaxy in a single tail. This second narrow filled tail is also unstable to KH instabilities. The flow in these regions becomes turbulent and forms vortices, and dissipates into the ICM within $t \simeq 1600$ Gyr. The ISM is completely stripped by $t \simeq 2400$ Gyr (seen in Figure 2). Figure 4 shows azimuthally averaged radial profiles of the gas density, temperature, pressure, and dark matter (particle) density from $t =$ 8–160 Myr.

3.2. Thermal Conduction, no Ram Pressure

In this section we discuss the effect of thermal conduction between the ICM and the ISM, conduction within the galaxy, and the subsequent evaporation of a galactic corona. We performed a simulation of the $2.8 \times 10^{11}\,M_\odot$ galaxy embedded in a static ICM, with $\boldsymbol{v}_{\rm ICM} = 0\,{\rm km\,s^{-1}}$. The other ICM parameters are the same as above.

Figure 5 shows radial profiles of the absolute values of the effective heat flux, as well as the theoretically expected saturated heat flux and full Spitzer heat flux calculated from the density and temperature of the fluid at approximately $t = 8$ Myr, $t = 63$ Myr, $t = 95$ Myr, and $t = 159$ Myr. Dashed lines indicate regions where the heat flux is positive (i.e., a negative temperature gradient), while solid lines show the typical situation where the heat flux is negative (i.e., inwardly directed). Note that the heat flux is only positive in regions where it is comparatively weak and where the temperature gradient is very close to zero (Figure 6). The magnitude of the heat flux depends strongly on the temperature and temperature gradient as $Q \propto T_{\rm e}^{5/2}\nabla T_{\rm e}$. Initially, at $t = 8$ Myr, the effective heat flux is highest inside the galaxy, where there is a nonzero temperature gradient, and decreases dramatically outside the galaxy ($r \gtrsim 100$ kpc) where the temperature profile is effectively flat. Within the galaxy, the effective heat flux depends sensitively on temperature and is

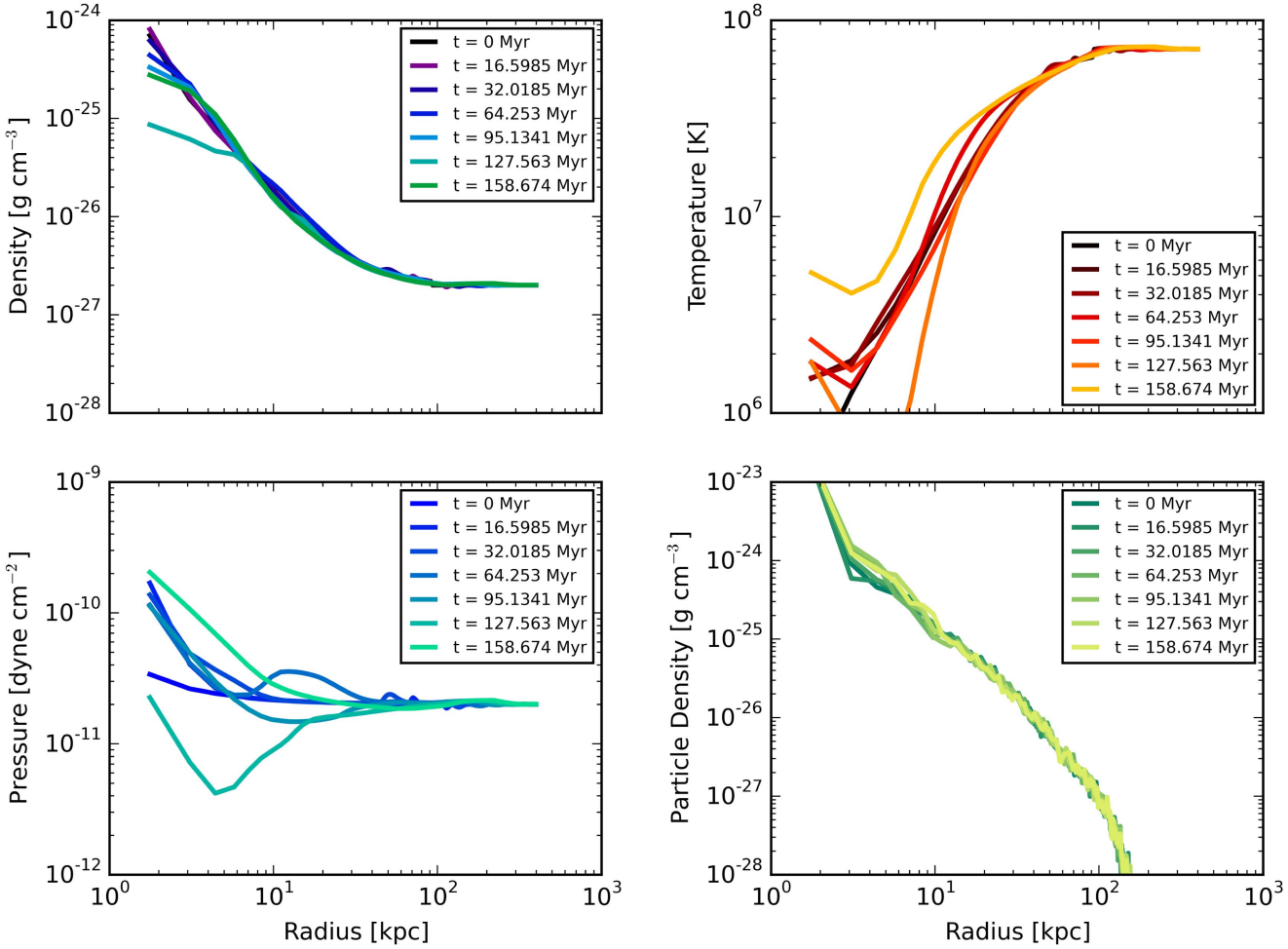

Figure 4. Profiles in a simulation with ram pressure but no thermal conduction.

significantly higher outside the cool galaxy core than within the core, i.e., at $r \gtrsim 10$ kpc.

Heat is transported from the ICM to the ISM and from the outer regions of the galaxy inward. As the ISM is heated, it expands. Figure 6 shows the evolution of density, temperature, and pressure profiles during the evaporation process. As heat is transported into the core, the core temperature increases, as do the density and pressure, which reach up to $t = 32$ Myr. From $t = 32$–96 Myr, the ISM density and pressure mostly decrease as the ISM expands, and the temperature increases up to the ICM temperature. After the initial expansion, gas flows back into the core, briefly resulting in an increased core density and pressure between $t = 140$–150 Myr. This gas then expands and evaporates outward; by $t = 160$ Myr, the density, temperature, and pressure profiles are fairly flat.

During this period of evaporation, the effective heat flux evolves considerably. At $t \simeq 55$–135 Myr, (Figure 5) the core gas temperature has increased to the extent that the effective heat flux, now saturated, is significantly higher than at early times. Heat is transported to the core ISM gas from the ISM in the outskirts and the ICM. There are three distinct radial zones in the galaxy: an inner classical zone, where the gas is still cool enough that the classical Spitzer heat flux is lower than the saturated flux ($r < 2$–5 kpc), an outer classical zone where the heat flux is primarily determined by the classical Spitzer heat flux since the temperature gradient is small ($r > 10$–20 kpc), and the intermediate saturated zone ($5 \lesssim r \lesssim 15$ kpc) where the temperature is sufficiently high and the temperature gradient is steep enough so the heat flux is saturated. Cowie & McKee (1977) describe these zones in their calculations of the evaporation of a cold gas cloud. For $t > 150$ Myr, when sufficient heat has been transported from the ICM so that the galaxy temperature profile is flat, the classical Spitzer heat flux is two orders of magnitude lower than the saturated heat flux.

The dark matter mass, which is an order of magnitude higher than the ISM mass, is mostly unaffected by the evaporation of the ICM, as seen in the particle density radial profile plot in Figure 6. The gravitational potential is primarily determined by the dark matter distribution, and therefore does not change either with the evaporation of gas. Therefore, to maintain hydrostatic equilibrium, the density and pressure gradients, while small, are nonzero. For $\Delta P = P(R_{200}) - P(0)$ and $\Delta\rho_{\rm gas} = \rho_{\rm gas}(R_{200}) - \rho_{\rm gas}(0)$, with $\Delta P \ll P$ and $\Delta\rho_{\rm gas} \ll \rho_{\rm gas}$, the equation of hydrostatic equilibrium can be written as

$$\frac{\Delta P}{R_{200}} \simeq \rho_{\rm gas}\frac{GM}{R_{200}^2}. \quad (16)$$

Additionally, the ideal gas law gives us

$$\Delta P = \frac{k_{\rm B}}{\mu m_{\rm p}}\Delta\rho_{\rm gas}T, \quad (17)$$

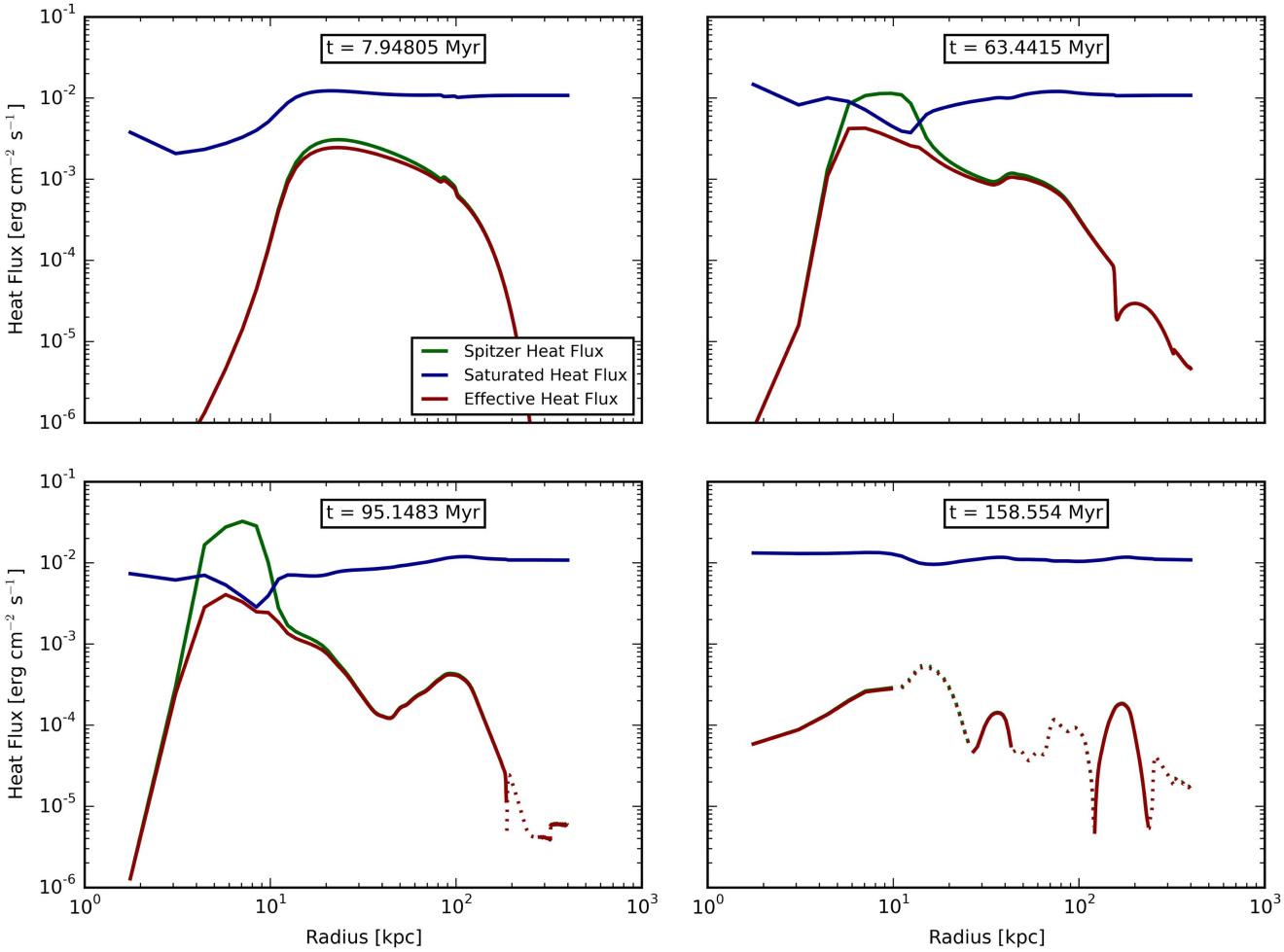

Figure 5. Profiles of the absolute values of the effective heat flux and expected theoretical values of saturated and classical Spitzer heat fluxes at different periods of the galaxy's evaporation. Solid lines correspond to a negative heat flux and dashed lines to a positive heat flux.

where we have dropped ΔT since $\Delta T/T \ll \Delta P/P$ and $\Delta T/T \ll \Delta\rho_{\rm gas}/\rho_{\rm gas}$. Therefore, we have

$$\frac{\Delta P}{P} \simeq \frac{\Delta\rho_{\rm gas}}{\rho_{\rm gas}}. \quad (18)$$

At $t = 400$ Myr, the density, pressure, and temperature profiles of the simulated galaxy correspond to $\frac{\Delta P}{P} \simeq \frac{\Delta\rho_{\rm gas}}{\rho_{\rm gas}} \simeq 0.02$, while $\frac{\Delta T}{T} \simeq 2 \times 10^{-4}$, consistent with our earlier assumptions of $\Delta T/T \ll \Delta P/P$ and $\Delta T/T \ll \Delta\rho_{\rm gas}/\rho_{\rm gas}$.

The heating, expansion, and evaporation of the ISM are seen in the density and temperature slices of Figure 7. We see the expanding shell of gas corresponding to the evaporating ISM at $t = 96$ Myr and $t = 160$ Myr. The galaxy's dense, cool core also visibly evaporates by $t = 160$ Myr.

Cowie & McKee (1977) determined the mass loss rate of a cool, spherical gas cloud of radius R, number density $\bar{n}_c$ with $T \sim 0$ at $r = R$, embedded in a hot medium with $T = T_f$ at $r \gg R$. Assuming classical evaporation with Spitzer conductivity, they showed that the evaporation timescale is

$$t_{\rm evap} = 3.3 \times 10^{20} \bar{n}_c R^2 T_f^{-5/2} \frac{\ln\Lambda}{30} {\rm Myr}. \quad (19)$$

For a gas cloud with the properties of the ISM in our simulated galaxy, where $R = R_{200}$ (in kpc) and $\bar{n_c} = M_{\rm gas}/(\frac{4}{3}\pi R_{200}^3 \times \mu m_{\rm p})$ $t_{\rm evap} = 216$ Myr, which is comparable to the actual evaporation timescale of $t = 160$ Myr. This evaporation timescale for gas flowing out from a cool cloud assumes steady state and does not include the effect of gravity. These assumptions do not hold for a galaxy with a potential gradient that is primarily determined by dark matter, which is not affected by thermal conduction. In our simulations, the galaxy's gravitational potential and gas are initially in hydrostatic equilibrium. As heat diffuses into the ISM, the ISM becomes isothermal and its density, pressure, and temperature profiles flatten, with a small gradient, but the ISM never evaporates completely. This simulation does not include the effect of ram pressure or tidal forces from the cluster gravitational potential, which are ultimately responsible for removing all of the ISM gas. However, we find that if thermal conduction with saturation is in fact effective, galaxies should not have prominent dense coronae.

3.3. Gas Loss from Thermal Conduction and Ram Pressure

We see in Section 3.1 that ram pressure alone removes the ISM by $t = 2$ Gyr, while isotropic thermal conduction results in the evaporation of the ISM by $t = 160$ Myr, as seen in Section 3.2. Therefore, evaporation that is due to thermal conduction is much more rapid than ram pressure stripping in removing gas. The presence of flowing ICM does qualitatively affect the process of evaporation that is due to thermal

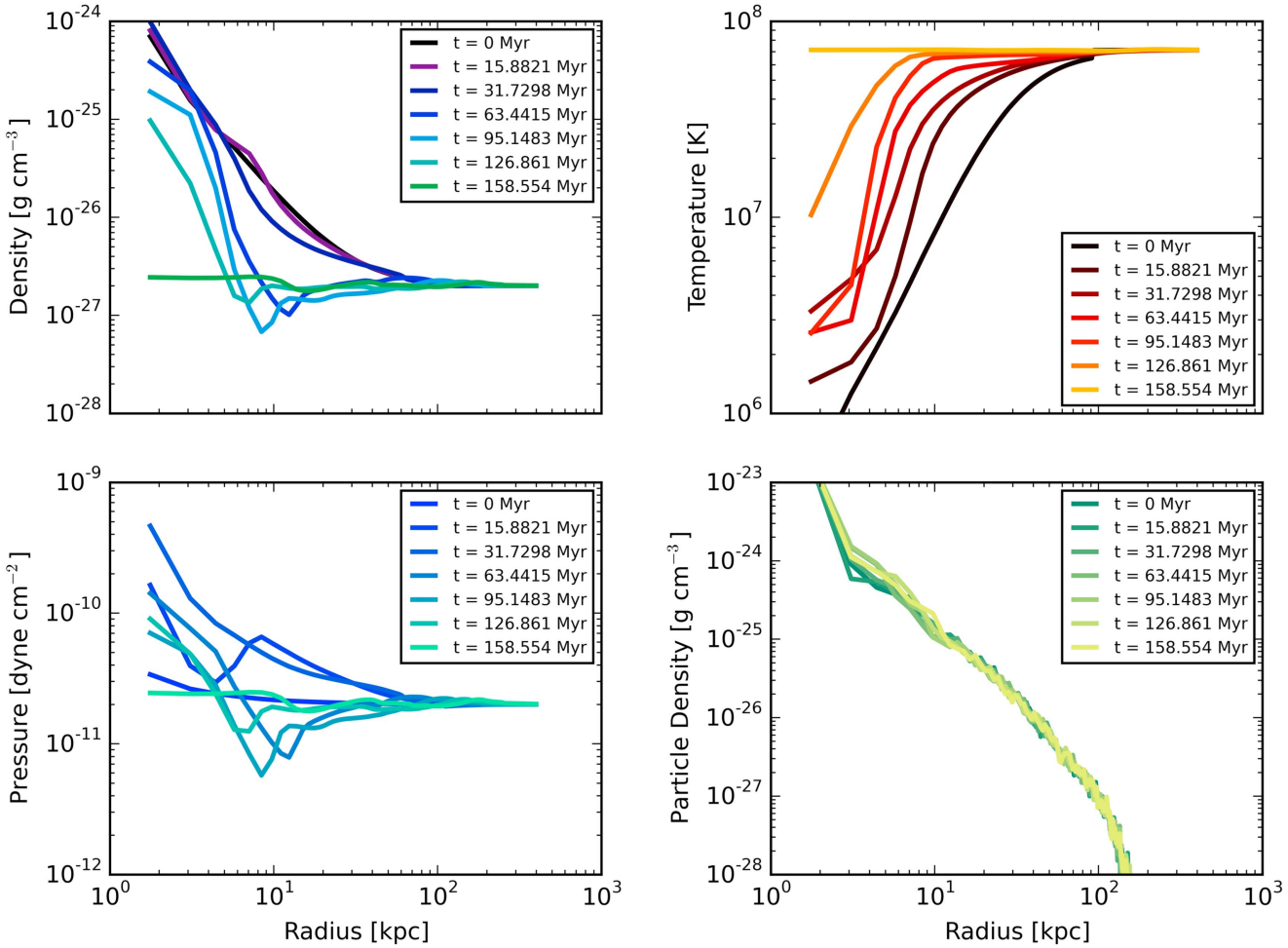

Figure 6. Profiles in a simulation of evaporation from thermal conduction but no ram pressure.

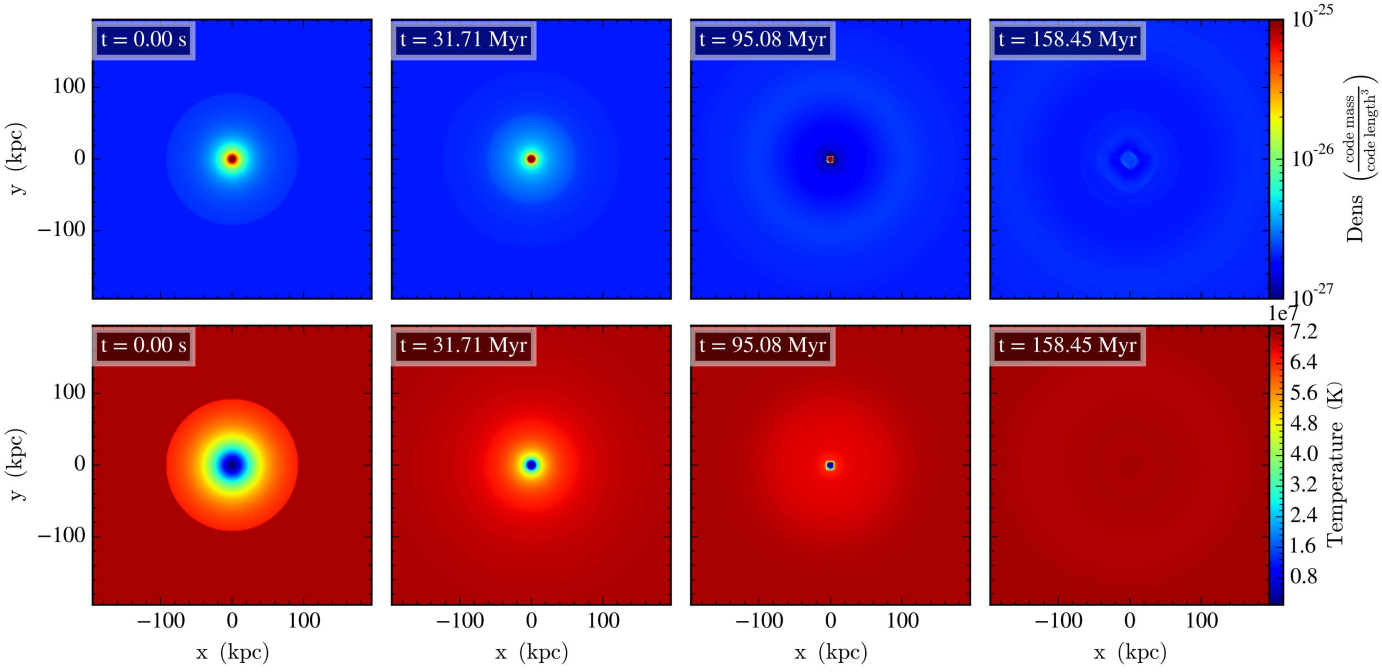

Figure 7. Slices of density and temperature in a simulation of evaporation from thermal conduction but no ram pressure.

conduction, however. Thermal conduction suppresses the formation of shear instabilities at the cool ISM—hot ICM interface, as heat is transported from the ICM to the outer edge of the ISM before KH instabilities develop. Thermal conduction broadens the transition region between the ISM and ICM, which smears out the velocity shear. This makes the ICM–ISM interface less KH unstable, particularly for the fastest growing, short-wavelength modes (Chandrasekhar 1961; Roediger et al. 2013a).

There is also a bow shock and a contact discontinuity, as in the simulation without thermal conduction. However, the nature of the bow shock is different in the presence of thermal conduction. A a result of rapid efficient heat transport, the shock is isothermal. This is seen in the density, temperature, and pressure jumps illustrated for both cases at $t = 40$ Myr in Figure 8. The shock front is visible in the density and pressure profiles at $x = -130$ kpc in the case with no conduction, and at $x = -115$ kpc in the case with thermal conduction. We see in Figure 8 that there is no temperature jump at the shock front in the presence of thermal conduction. Additionally, the contact discontinuity at $R_{200} = 90$ kpc at the ICM–ISM interface is clearly visible as a density jump with no corresponding pressure jump. The shock front in the case with conduction trails the shock in the absence of conduction, therefore the isothermal shock is slower than the adiabatic shock. The Mach numbers of the shocks in both cases are comparable, however. The Mach number of the adiabatic shock $M_{\rm adiabatic} = v_{\rm shock,adiabatic}/c_{\rm adiabatic}$, where the sound speed $c_{\rm adiabatic} = \sqrt{\gamma P/\rho}$, is $M_{\rm adiabatic} = 1.136$. The Mach number of the isothermal shock $M_{\rm isothermal} = v_{\rm shock,isothermal}/c_{\rm isothermal}$, where the sound speed $c_{\rm isothermal} = \sqrt{P/\rho}$, is $M_{\rm isothermal} = 1.145$.

The bow shock expands outward and dissipates, while the galaxy core gas evaporates as a result of thermal conduction. The core evaporates before ram pressure strips it away. The reverse shock passes through the evaporating and close to isothermal core and converges behind it. This reverse shock then expands outward in a thin shell, eventually dissipating by $t \simeq 200$ Myr. The galaxy core evaporates before the expanding reverse shock passes through it. Compared to a gas loss timescale of $t = 2000$ Myr due to ram pressure stripping alone, in the presence of thermal conduction, the galaxy's ISM has evaporated by $t = 200$ Myr; the remnant gas in the galaxy potential well is isothermal with the ICM, with a small gradient in the density and pressure profiles. This gas, as in Section 3.2, never has a completely flat density and temperature profile as long as hydrostatic equilibrium is effective. Of course, in real clusters, tidal and other gravitational effects will flatten the potential and remove gas in addition to any evaporation from thermal conduction.

The evolution of density, pressure, temperature, and dark matter density profiles of this galaxy are shown in Figure 9. These azimuthally averaged profiles are nearly identical to the evolution of fluid variable profiles in Figure 6, showing that the presence of an ICM wind and strong ram pressure is not as effective at removing gas as isotropic saturated thermal conduction.

3.4. Varying Galaxy Mass and ICM Density

To test the qualitative and quantitative variations in the evaporation of galaxies from thermal conduction, we performed a simulation of a galaxy 10 times more massive than our base model, and of our standard lower mass galaxy in a low-density low-pressure ICM of the same temperature. These are lower resolution simulations, corresponding to a maximum spatial resolution of 2.53 kpc, a factor of two higher than the 1.26 kpc resolution in the previously described simulations. This resolution is still significantly smaller than the ICM mean free path, and the overall results are unaffected.

3.4.1. High Mass Galaxy

We simulated the evaporation of a $2.8 \times 10^{12}\,M_\odot$ galaxy in an ICM wind tunnel identical to the previous simulations. This galaxy has a virial radius $R_{200} = 190$ kpc. To adequately capture the expanding bow shock, we use a larger simulation box of side 1296 kpc in which all of the spatial dimensions are twice as large as in the earlier simulations. Although the average ISM density as well as the ICM density, pressure, and temperature are identical to the previous runs, the larger galaxy size affects the evaporation timescale. The overall evaporation time should scale, approximately, as $t_{\rm evap} \propto M_{\rm gas}/R_{200}$ (Equation (19)). Compared to the standard galaxy model, this galaxy's mass is 10 times higher, and its radius is twice as large, therefore the evaporation time should be approximately five times longer. The total evaporation time for this galaxy is $t \simeq 555$ Myr, while the evaporation time for the fiducial galaxy is $t \simeq 160$ Myr. This timescale is still significantly lower than the ram pressure stripping timescale. The evaporation time is $\sim 3.5\times$ higher for the massive galaxy. This is consistent with the analytically idealized predictions of Equation (19), where at a given density and ICM temperature, $t_{\rm evap} \propto R^2$. The virial radii of the fiducial galaxy and massive galaxy are $R_{200} = 92$ kpc and $R_{200} = 190$ kpc, respectively, therefore the evaporation time will scale by a factor of $\sim 2^2 = 4$.

The evolution of the ISM is seen in azimuthally averaged profiles of density and temperature and slices of density in Figures 10 and 11. The timesteps at which density and temperature values are shown here are different from those in the previous runs, since the overall evaporation time is higher. Qualitatively, the evolution of the ISM is similar to that in the galaxy in Section 3.3. There is an initial contact discontinuity at the ISM-ICM interface on the side of the galaxy facing the ICM wind. A bow shock propagates outward into the ICM, while a reverse shock propagates into the galaxy. The reverse shock converges behind the core, then expands outward. Through this process, the ISM is also heated through thermal conduction with the ICM and continues to expand. In the simulations in Sections 3.2 and 3.3, the galaxy core evaporates before the expanding reverse shock, after converging behind the galaxy, passes through the core. The massive galaxy core, however, does not evaporate until after the shock passes. The expanding reverse shock passes through the core at $t \simeq 325$ Myr. The core expands and evaporates at $t = 515$ Myr, forming a low-density cavity; this evacuated zone is soon filled with inflowing ISM gas, and by $t = 555$ Myr, the ISM has flat density, pressure, and temperature profiles. As in the earlier runs, the dark matter density profile is largely unaffected.

3.4.2. Low-density ICM

We performed a simulation of the $2.8 \times 10^{11}\,M_\odot$ galaxy in an ICM wind tunnel with $\rho_{\rm ICM} = 2 \times 10^{-28}$ g cm^{-3}, $P_{\rm ICM} = 2 \times 10^{-12}$ erg cm^{-3}, and $T_{\rm ICM}$ identical to the previous simulations at 7.14×10^7 K. The ICM wind speed is

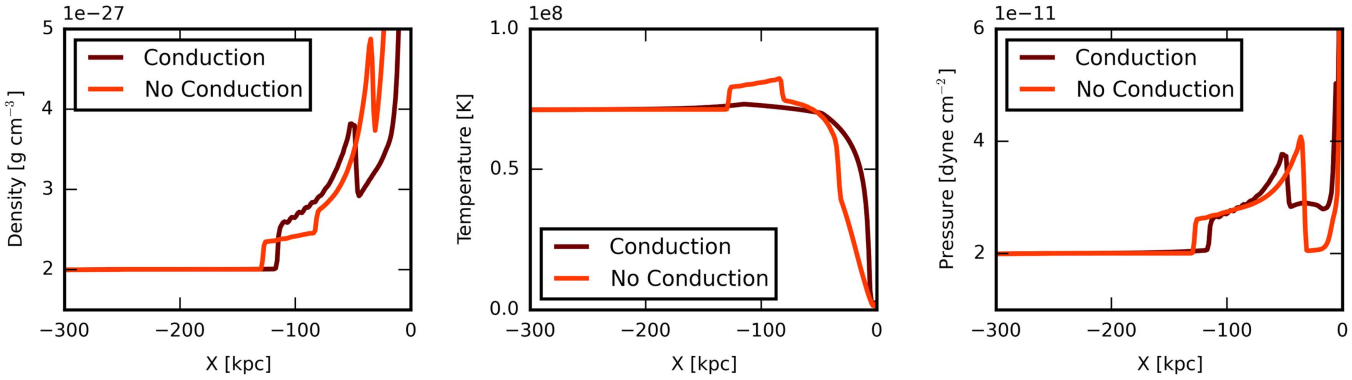

Figure 8. Density, temperature, and pressure along the x-axis showing the presence of the shock and contact discontinuity in simulations with ram pressure, in the presence or absence of thermal conduction at $t = 40$ Myr.

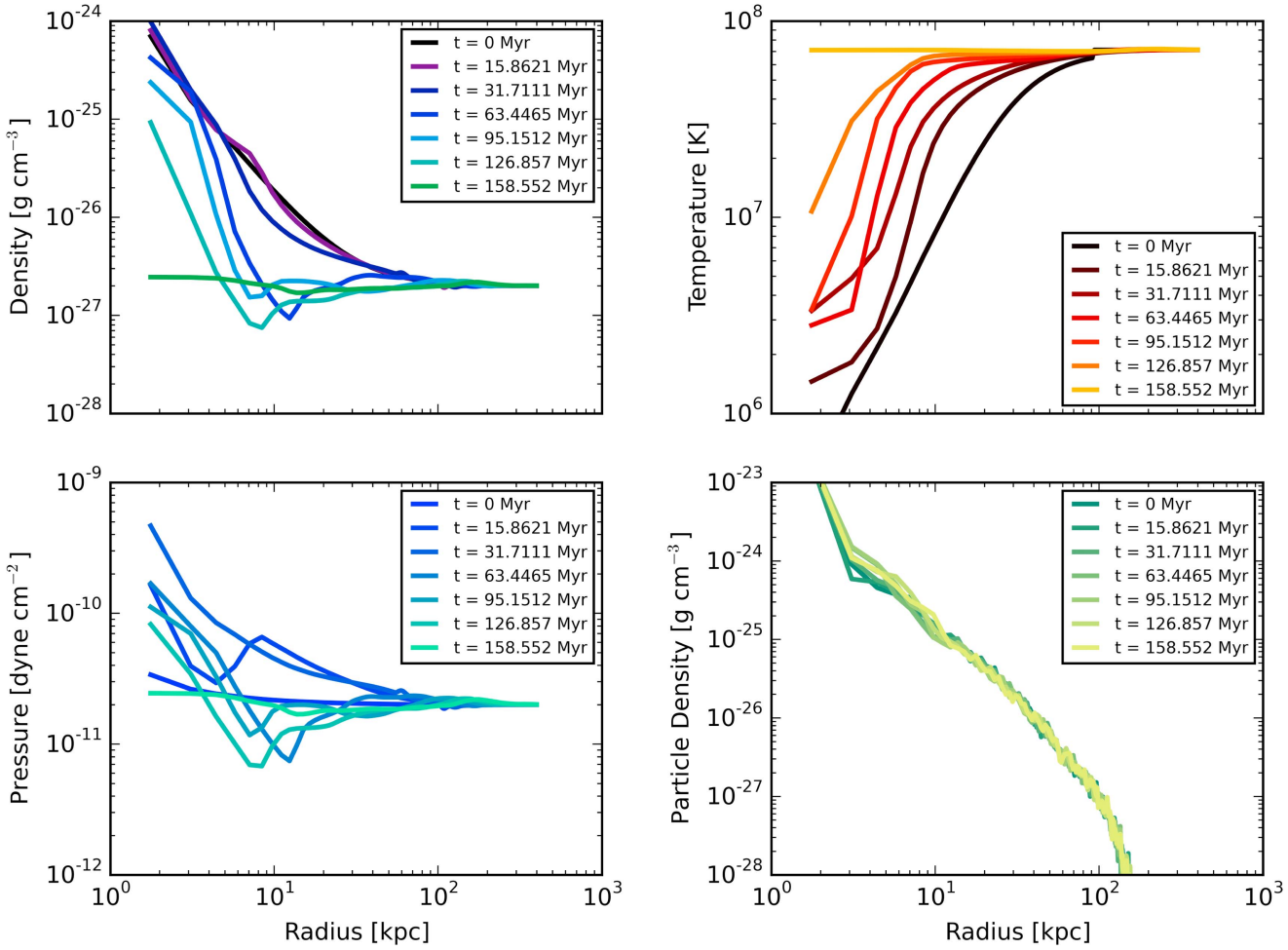

Figure 9. Profiles in a simulation of evaporation from thermal conduction with ram pressure.

$v_{\rm ICM} = 610\,{\rm km\,s^{-1}}$, and this simulation includes saturated thermal conduction. Since the ISM density profile is initialized to be continuous with the ICM density, the density in the galaxy outskirts is lower than in the previous simulation; the pressure profile is also modified to maintain hydrostatic equilibrium. Subsequently, the temperature in the galaxy outskirts is lower than in the ISM in our earlier simulations, seen when comparing the $t = 0$ Myr temperature profiles in Figure 6.

The cooler ISM and lower density lead to lower heat fluxes through thermal conduction. This is seen in Figure 12, which shows radial profiles of the effective, classical, and saturated heat fluxes at $t = 64$ and $t = 160$ Myr. The typical effective heat fluxes at these times are $|\boldsymbol{Q}_{\rm eff}| \simeq 10^{-4} - 10^{-3}\,{\rm erg\,cm^{-2}\,s^{-1}}$, while in the high-density ICM, $|\boldsymbol{Q}_{\rm eff}| \simeq 10^{-3} - 10^{-2}\,{\rm erg\,cm^{-2}\,s^{-1}}$ at $t = 63$ Myr. At $t = 160$ Myr the ISM has evaporated in the high-density ICM, and there is no temperature gradient. Additionally, since the ICM wind speed is unchanged while the

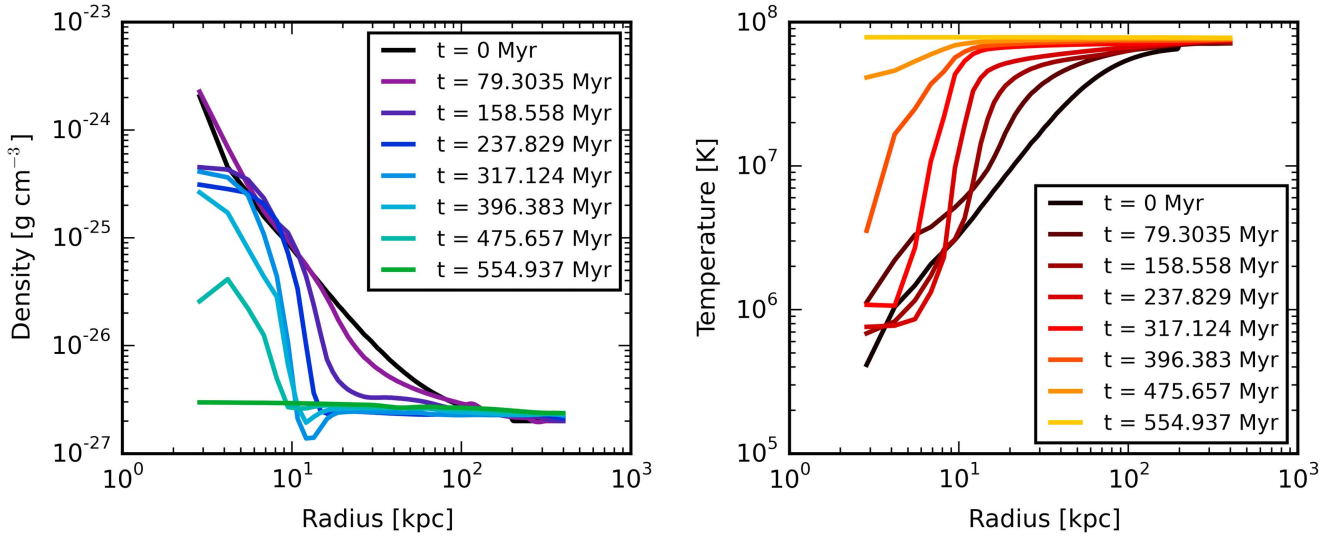

Figure 10. Profiles of gas density and temperature in a simulation of evaporation from thermal conduction with ram pressure for a more massive galaxy.

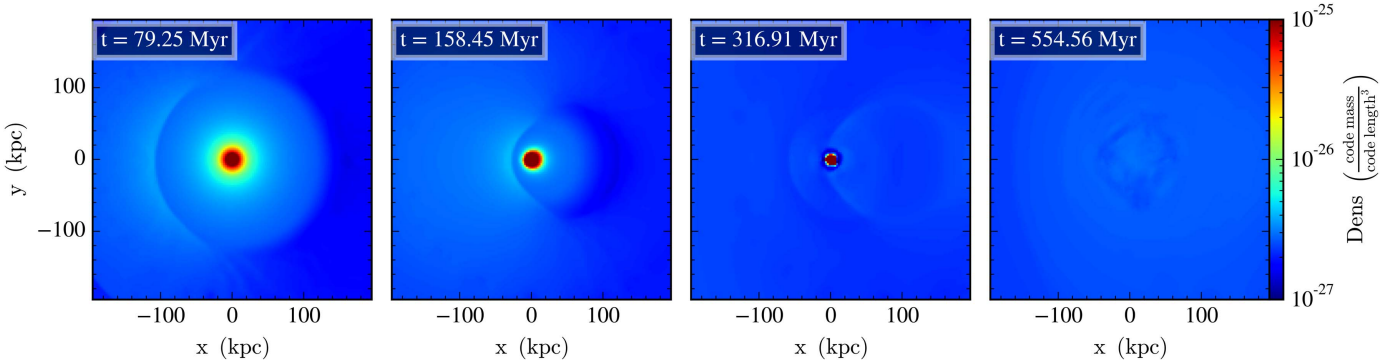

Figure 11. Slices of the gas density in a simulation of evaporation from thermal conduction with ram pressure for a $2.8 \times 10^{12}\,M_{\odot}$ massive galaxy.

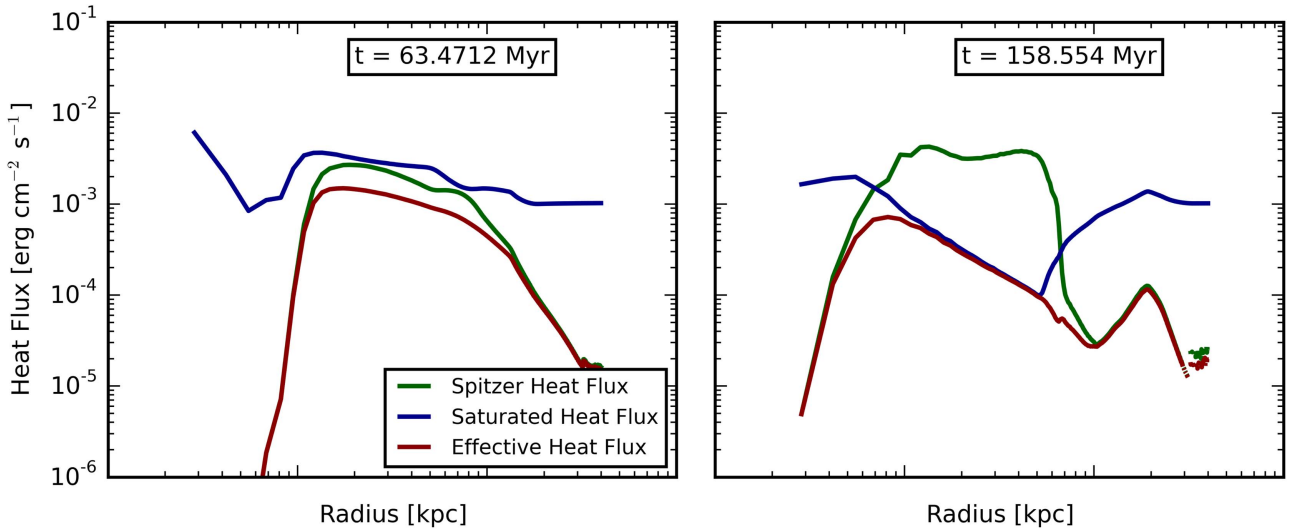

Figure 12. Profiles of the effective heat flux and expected theoretical values of saturated and classical Spitzer heat fluxes at different periods of the galaxy evaporation in the low-density ICM.

ICM density is lower by an order of magnitude, the ram pressure is also reduced by an order of magnitude. The net result is that at lower heat fluxes, the rate of evaporation of the galaxy is much lower; the time it takes for the galaxy to evaporate is $t \simeq 350$ Myr. Qualitatively, the evolution of the ISM (Figure 13) is similar to the high-density ICM case, seen in Figure 14: an initial shock wave is formed at the ICM–ISM interface and propagates out into the ICM. The ISM expands as it is heated, and the density outside the core drops rapidly. The galaxy core evaporates by $t = 250$ Myr. The ICM reverse shock

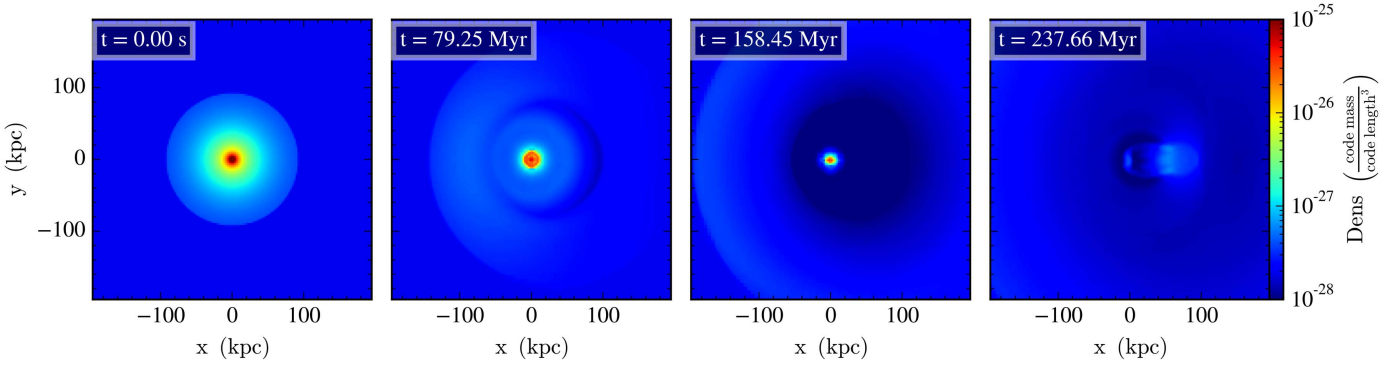

Figure 13. Slices of gas density in a simulation of evaporation from thermal conduction with ram pressure for a lower ICM density.

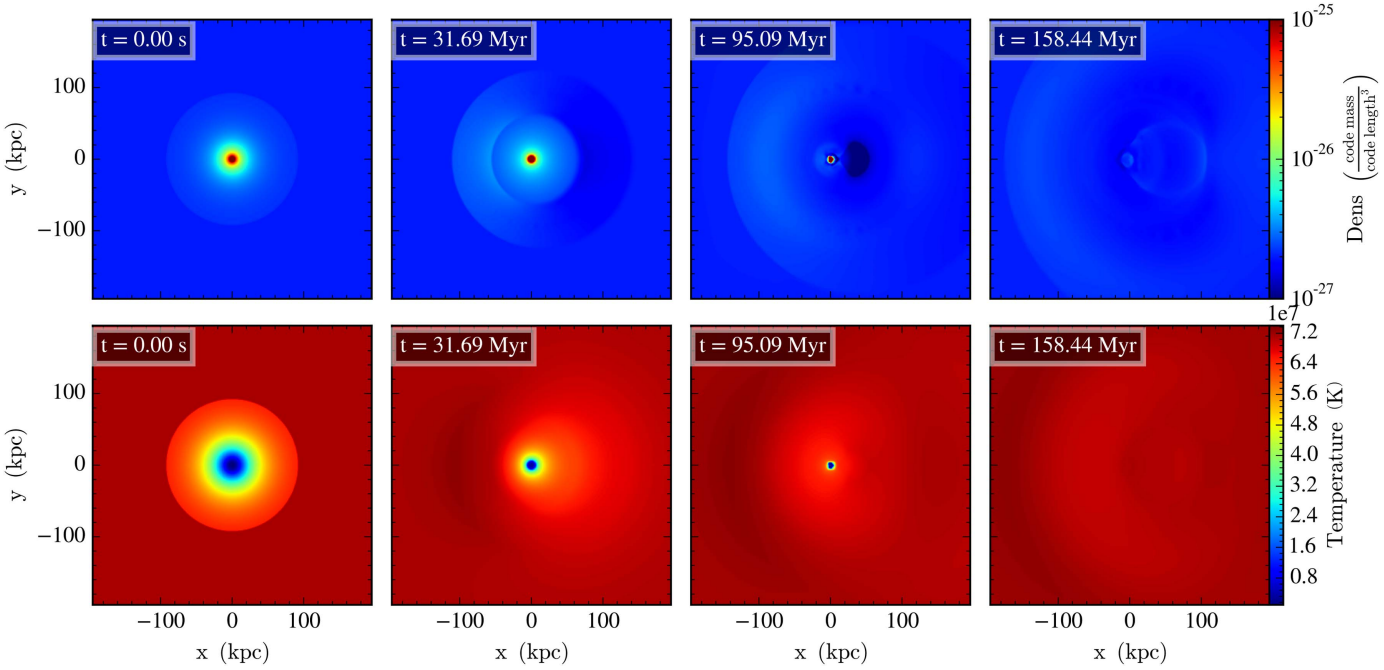

Figure 14. Slices of density and temperature in a simulation of evaporation from thermal conduction with ram pressure.

converges behind the galaxy core, then expands and dissipates. The time evolution of the density profile is also seen in Figure 15.

4. Discussion

Galactic hot coronae evaporates on $\sim 10^2$ Myr timescales in the presence of isotropic thermal conduction including saturation in the ICM. Specifically, in the simulations here, evaporation times are ∼160 Myr for the $2.8 \times 10^{11}\,M_\odot$ galaxy, and ∼550 Myr for the $2.8 \times 10^{12}\,M_\odot$ galaxy. Ram pressure strips gas on much longer timescales. The gas loss time from to ram pressure stripping alone, in an identical ICM, is ∼2.5 Gyr for the $2.8 \times 10^{11}\,M_\odot$ galaxy; the simulated galaxies evaporate as a result of conduction alone well before ram pressure can be effective. Qualitatively, by comparing the effects of evaporation from conduction in Sections 3.2 and 3.3, we see that the additional effect of ICM ram pressure is to form an isothermal bow shock as well as a reverse shock; evaporation rates are nearly identical in both cases. In the absence of ICM wind and ram pressure, there is no bow shock or reverse shock. Even when the conductive heat flux is much reduced, as in the lower density ICM, the complete evaporation time is ∼300 Myr for the $2.8 \times 10^{11}\,M_\odot$ galaxy. Efficient thermal conduction therefore results in the rapid evaporation of the galaxies' hot X-ray emitting coronae, including their cool dense cores.

Galaxies moving relative to the ICM at higher velocities will experience stronger ram pressure as $P_{\rm ram} \propto v_{\rm ICM}^2$. However, the thermal evaporation timescales are more than an order of magnitude shorter than the stripping timescales in our simulations. Thus, speeds greater than $2000\,{\rm km\,s^{-1}}$ would probably be required for ram pressure stripping to become competitive with thermal evaporation, all other things being equal. Higher galaxy speeds are expected in more massive clusters, but these also have higher gas temperatures, with $kT \propto v_{\rm ICM}$. Since the thermal conduction and evaporation timescales decrease much faster than linearly with T (e.g., Equation (19)), the dominance of thermal evaporation is actually expected to be stronger in clusters with higher galaxy velocities.

In addition to the evaporation of coronae and central cores, thermal conduction suppresses shear instabilities at the ISM-ICM interface and prevents the formation of stripped tails. In the absence of conduction, ram pressure pushes on the ISM in the direction of the ICM wind, stripping the ISM away from the galaxy. Stripped ISM gas trails the galaxy, forming KH

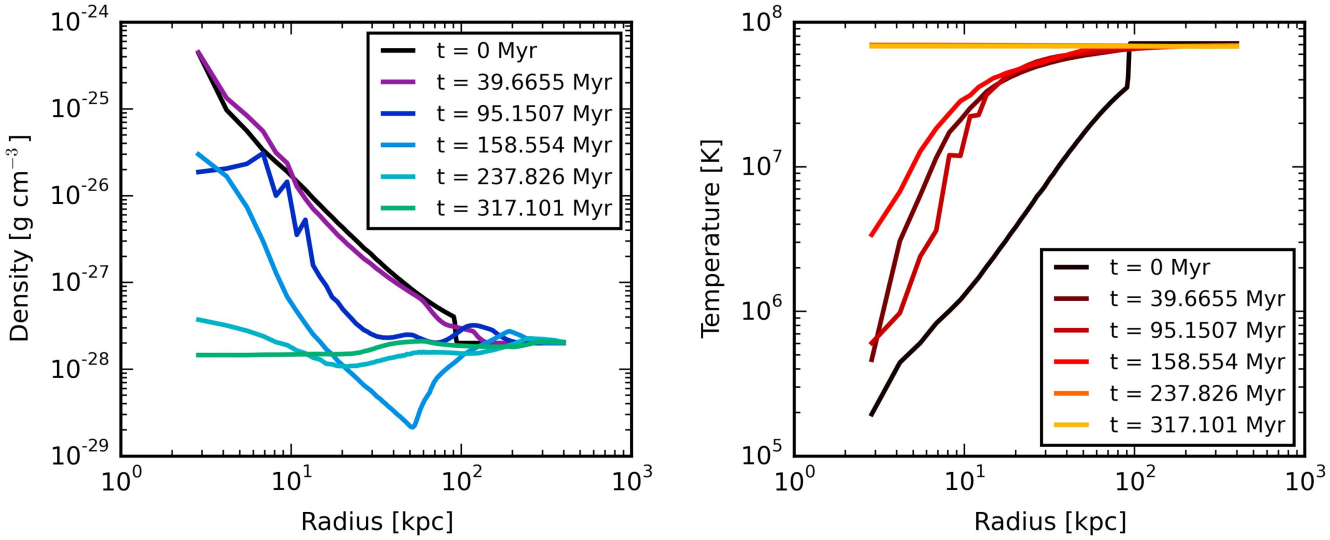

Figure 15. Profiles of gas density and temperature in a simulation of evaporation from thermal conduction with ram pressure for a lower ICM density.

instabilities at the ICM interface. The galaxies' core ISM gas is subject to ram pressure once the outer ISM has been peeled away, and it gradually dissipates. In our simulated galaxy, the formation of the initial tail takes $t \sim$ 300–400 Myr (Figure 2). The total evaporation timescale for the same galaxy is $t = 160$ Myr, therefore stripped galaxies will not be able to form tails if thermal conduction is efficient. Even in the lower density ICM simulation, where thermal conduction is slower, there is no stripped tail. The complete suppression of the formation of hot X-ray emitting tails is in direct contradiction with observed X-ray tails in cluster galaxies (e.g., Forman et al. 1979; Irwin & Sarazin 1996; Sun & Vikhlinin 2005; Machacek et al. 2006; Kim et al. 2008; Randall et al. 2008; Sun et al. 2010; Kraft et al. 2011; Zhang et al. 2013).

In addition to the absence of stripped tails, thermal conduction results in the rapid removal of the galaxies' central coronae. The evaporation and absence of coronae is also in tension with observations of compact X-ray emitting coronae in a large fraction of group galaxies ($\sim$80% of $L_K > L_*$ galaxies; Jeltema et al. 2008) and cluster galaxies ($\sim$60% of $L_K > 2L_*$ galaxies; Sun et al. 2007). The frequency of these observations suggests that observed coronae are long lived, i.e., they survive stripping and evaporation for many Gyr. Given the prevalence of stripped tails and X-ray emitting coronae, isotropic thermal conduction is therefore likely ineffective in ICM–ISM interactions in real clusters. The temperature and density structure of the ICM and hot ISM result in temperature gradients and electron mean free paths that favor efficient thermal conduction. Evaporation must therefore be contained, or any gas loss must be rapidly and continually replenished given the long lifetimes of these coronae.

Comparing the ram pressure stripping time ($\sim$2 Gyr) with the evaporation time ($\sim$150 Myr) for our simulated galaxy, we estimate that thermal conduction must be suppressed by at least a factor of 10-20 to explain the observed X-ray tails in clusters, and considerably longer to sustain observed X-ray coronae for several Gyr. Vikhlinin et al. (2001) estimate that conductivity must be suppressed by a factor of $\sim$100$\times$ for the cooling rate calculated from the X-ray emissivity for the central coronae in their paper. A more extensive review and calculations by Sun et al. (2007) for satellite galaxy coronae also show that conduction must be suppressed by a factor of $\sim$20-100 in observed coronae. For the survival of observed cold fronts in clusters, calculations based on mean free path arguments, reviewed by Markevitch & Vikhlinin (2007), require suppression factors of at least 3-4.

The presence of magnetic fields and the subsequent anisotropic thermal conduction along magnetic field lines (as opposed to isotropic thermal conduction) dramatically reduces evaporation rates; overall, ISM evaporation timescales are comparable to ram pressure stripping timescales. We explore the effects of anisotropic thermal conduction in detail in Paper II. To understand the survival of coronae around central galaxies in the Coma cluster, Vikhlinin et al. (2001) hypothesize that radiative cooling can in principle offset evaporation if the rate at which gas cools is equal to the heating rate. The general applicability of this process is debatable since it requires identical heating and cooling rates to prevent either process completely destroying central coronae.

In addition to the evaporation of galactic coronae, thermal conduction has other effects on the evolution of the ICM. Jubelgas et al. (2004) and Dolag et al. (2004) find using SPH cosmological simulations of cluster formation that thermal conduction results in flat temperature profiles in the cores of simulated clusters and a smoother temperature distribution in the ICM. Smith et al. (2013) find using grid-based numerical simulations that isotropic conduction results in isothermal cluster cores, but not in a significant reduction in temperature inhomogeneity. These simulations did not explicitly include magnetic fields; we discuss the additional effects of magnetic fields and anisotropic thermal conduction on the ICM in Paper II.

5. Conclusions

We performed simulations of the loss of gas from galaxies moving relative to the ICM ($\rho_{\rm ICM} = 2 \times 10^{-27}$ g cm^{-3}, $T_{\rm ICM} = 7.14 \times 10^7$ K, $v_{\rm galaxy,\ ICM} = 610$ km s^{-1}) as a result of ram pressure and thermal conduction. The primary objective of these simulations was to quantify the effect of isotropic saturated thermal conduction on the evaporation of the cluster galaxy gas. Using simulations without conduction, we characterized the effects of ram pressure alone: a bow shock and reverse shock are initially driven from the ISM-

ICM interface, the reverse shock converges behind the core of the galaxy before expanding outward, KH instabilities are formed at this interface as the ICM flows past the ICM, the force due to ram pressure gradually unbinds the ISM from the ICM, and the ISM trails the galaxy in a tail of gas that dissipates in the ISM over a total timescale of $t = 2 - 3$ Gyr for a $2.8 \times 10^{11} M_{\odot}$ galaxy.

Thermal conduction, in the absence of ram pressure, results in the transport of heat from the ICM to the ISM; as a result, the outer ISM initially expands and evaporates, with an increase in temperature and decrease in density and pressure. The cooler denser core is then heated; eventually, the ISM and the ICM are isothermal. The classical heat flux $Q \propto T_{\rm e}^{5/2} \nabla T$, while the saturated heat flux $Q_{\rm sat} \propto T^{3/2}$ and is independent of the temperature gradient. As the ISM evaporates, thermal conduction is briefly saturated within the galaxy when the outer ISM is heated to high temperatures, which results in a steep temperature gradient within the ISM. During this period, there is an inner classical zone of low-temperature gas, an intermediate zone of hot, high-temperature gradient gas, and an outer classical zone of hot, low-temperature gradient gas. The background galaxy potential is unaffected in our simulations, particularly since we do not include the cluster gravitational potential, therefore hydrostatic equilibrium forces a low temperature, density, and pressure gradient. The evaporation time for the hot ISM is $t = 160$ Myr for a $2.8 \times 10^{11} M_{\odot}$ galaxy.

In the presence of ram pressure and isotropic thermal conduction, gas loss is largely driven by evaporation, a much faster process than ram pressure stripping. A bow shock and reverse shock propagate in these simulations, in the presence of conduction, although the bow shock is isothermal and not adiabatic, and the galaxy's core evaporates before the converged reverse shock propagates outward.

For a more massive $2.8 \times 10^{12} M_{\odot}$ galaxy in an identical ICM wind, the process of evaporation and stripping is largely similar, although the evaporation time is $t = 550$ Myr. Qualitatively, the only significant difference in the evaporation process is that the galaxy core does not evaporate before the expansion of the reverse shock. We also simulated the evaporation of a $2.8 \times 10^{11} M_{\odot}$ galaxy in a low-density ICM of the same temperature ($\rho_{\rm ICM} = 2 \times 10^{-28}$ g cm^{-3}, $T_{\rm ICM} = 7.14 \times 10^{7}$ K). Owing to the smaller heat flux, the evaporation time increases to $t \simeq 300$ Myr.

We therefore find that under realistic ICM and ISM conditions, isotropic thermal conduction efficiently removes the ISM at a significantly faster rate than ram pressure stripping. The removed ISM gas does not form tails, since it expands and evaporates reaching the temperature and density of the ICM before tails can form. In addition to the rapid removal of gas, thermal conduction suppresses the formation of KH instabilities. The existence of hot galactic coronae and stripped X-ray emitting tails in cluster galaxies therefore requires that thermal conduction is suppressed, likely as a result of ICM magnetic fields, which in these conditions force thermal conduction to be effectively anisotropic, i.e., confine heat to flow along magnetic field lines only.

R.V. was supported by an NSF Astronomy and Astrophysics Postdoctoral Fellowship under award AST-1501374 and partially by the NASA *Chandra* theory award TM5-16008X. C.L.S. was supported in part by NASA *Chandra* grants GO5-16131X and GO5-16146X and NASA *XMM-Newton* grants NNX15AG26G, NNX16AH23G, and NNX17AC69G. The simulations presented here were carried out on the Rivanna cluster at the University of Virginia. FLASH was developed largely by the DOE-supported ASC/Alliances Center for Astrophysical Thermonuclear Flashes at the University of Chicago. The figures in this paper were generated using the `yt` software package (Turk et al. 2011). We thank the anonymous referee for useful comments that helped improve this paper.

References

Bertschinger, E., & Meiksin, A. 1986, ApJL, 306, L1
Boselli, A., & Gavazzi, G. 2006, PASP, 118, 517
Carilli, C. L., & Taylor, G. B. 2002, ARA&A, 40, 319
Chandrasekhar, S. 1961, Hydrodynamic and Hydromagnetic Stability (Oxford: Clarendon)
Cortese, L., Catinella, B., Boissier, S., Boselli, A., & Heinis, S. 2011, MNRAS, 415, 1797
Cowie, L. L., & McKee, C. F. 1977, ApJ, 211, 135
Cowie, L. L., & Songaila, A. 1977, Natur, 266, 501
Davies, R. D., & Lewis, B. M. 1973, MNRAS, 165, 231
Dolag, K., Jubelgas, M., Springel, V., Borgani, S., & Rasia, E. 2004, ApJL, 606, L97
Dressler, A. 1980, ApJ, 236, 351
Dubey, A., Reid, L. B., & Fisher, R. 2008, PhyS, 2008, 014046
Forman, W., Schwarz, J., Jones, C., Liller, W., & Fabian, A. C. 1979, ApJL, 234, L27
Fryxell, B., Olson, K., Ricker, P., et al. 2000, ApJS, 131, 273
Ghizzardi, S., Molendi, S., Pizzolato, F., & De Grandi, S. 2004, ApJ, 609, 638
Gnedin, O. Y. 2003a, ApJ, 589, 752
Gnedin, O. Y. 2003b, ApJ, 582, 141
Gómez, P. L., Nichol, R. C., Miller, C. J., et al. 2003, ApJ, 584, 210
Govoni, F., & Feretti, L. 2004, IJMPD, 13, 1549
Gunn, J. E., & Gott, J. R., III 1972, ApJ, 176, 1
Haines, C. P., Pereira, M. J., Smith, G. P., et al. 2013, ApJ, 775, 126
Haynes, M. P., & Giovanelli, R. 1984, AJ, 89, 758
Irwin, J. A., & Sarazin, C. L. 1996, ApJ, 471, 683
Jaffé, Y. L., Verheijen, M. A. W., Haines, C. P., et al. 2016, MNRAS, 461, 1202
Jeltema, T. E., Binder, B., & Mulchaey, J. S. 2008, ApJ, 679, 1162
Jubelgas, M., Springel, V., & Dolag, K. 2004, MNRAS, 351, 423
Kapferer, W., Sluka, C., Schindler, S., Ferrari, C., & Ziegler, B. 2009, A&A, 499, 87
Kawata, D., & Mulchaey, J. S. 2008, ApJL, 672, L103
Kazantzidis, S., Magorrian, J., & Moore, B. 2004, ApJ, 601, 37
Kennicutt, R. C., Jr. 1983, AJ, 88, 483
Kim, D.-W., Kim, E., Fabbiano, G., & Trinchieri, G. 2008, ApJ, 688, 931
Kraft, R. P., Forman, W. R., Jones, C., et al. 2011, ApJ, 727, 41
Kronberg, P. P. 2005, in Cosmic Magnetic Fields, ed. R. Wielebinski & R. Beck (Bristol: IOP), 9
Larson, R. B., Tinsley, B. M., & Caldwell, C. N. 1980, ApJ, 237, 692
Lewis, I., Balogh, M., De Propris, R., et al. 2002, MNRAS, 334, 673
Machacek, M., Jones, C., Forman, W. R., & Nulsen, P. 2006, ApJ, 644, 155
MacNeice, P., Olson, K. M., Mobarry, C., de Fainchtein, R., & Packer, C. 2000, CoPhC, 126, 330
Markevitch, M., & Vikhlinin, A. 2007, PhR, 443, 1
Mastropietro, C., Moore, B., Mayer, L., et al. 2005, MNRAS, 364, 607
McCarthy, I. G., Frenk, C. S., Font, A. S., et al. 2008, MNRAS, 383, 593
McNamara, B. R., & Nulsen, P. E. J. 2007, ARA&A, 45, 117
Moore, B., Katz, N., Lake, G., Dressler, A., & Oemler, A. 1996, Natur, 379, 613
Moore, B., Lake, G., & Katz, N. 1998, ApJ, 495, 139
Narayan, R., & Medvedev, M. V. 2001, ApJL, 562, L129
Navarro, J. F., Frenk, C. S., & White, S. D. M. 1997, ApJ, 490, 493
Postman, M., & Geller, M. J. 1984, ApJ, 281, 95
Quilis, V., Moore, B., & Bower, R. 2000, Sci, 288, 1617
Randall, S., Nulsen, P., Forman, W. R., et al. 2008, ApJ, 688, 208
Rasmussen, J., Mulchaey, J. S., Bai, L., et al. 2012, ApJ, 757, 122
Ricker, P. M. 2008, ApJS, 176, 293
Roediger, E., Brüggen, M., & Hoeft, M. 2006, MNRAS, 371, 609
Roediger, E., Kraft, R. P., Forman, W. R., Nulsen, P. E. J., & Churazov, E. 2013a, ApJ, 764, 60
Roediger, E., Kraft, R. P., Nulsen, P., et al. 2013b, MNRAS, 436, 1721
Roediger, E., Kraft, R. P., Nulsen, P. E. J., et al. 2015a, ApJ, 806, 103

Roediger, E., Kraft, R. P., Nulsen, P. E. J., et al. 2015b, ApJ, 806, 104
Ruszkowski, M., Brüggen, M., Lee, D., & Shin, M.-S. 2014, ApJ, 784, 75
Ryu, D., Schleicher, D. R. G., Treumann, R. A., Tsagas, C. G., & Widrow, L. M. 2012, SSRv, 166, 1
Sanders, J. S., Fabian, A. C., Sun, M., et al. 2014, MNRAS, 439, 1182
Sarazin, C. L. 1986, RvMP, 58, 1
Schulz, S., & Struck, C. 2001, MNRAS, 328, 185
Shin, M.-S., & Ruszkowski, M. 2014, MNRAS, 445, 1997
Smith, B., O'Shea, B. W., Voit, G. M., Ventimiglia, D., & Skillman, S. W. 2013, ApJ, 778, 152
Solanes, J. M., Manrique, A., García-Gómez, C., et al. 2001, ApJ, 548, 97
Spitzer, L. 1962, Physics of Fully Ionized Gases (New York: Interscience)
Spitzer, L., & Härm, R. 1953, PhRv, 89, 977
Sun, M., Donahue, M., Roediger, E., et al. 2010, ApJ, 708, 946
Sun, M., Jerius, D., & Jones, C. 2005a, ApJ, 633, 165
Sun, M., Jones, C., Forman, W., et al. 2007, ApJ, 657, 197
Sun, M., & Vikhlinin, A. 2005, ApJ, 621, 718
Sun, M., Vikhlinin, A., Forman, W., Jones, C., & Murray, S. S. 2005b, ApJ, 619, 169
Tonnesen, S., & Bryan, G. L. 2009, ApJ, 694, 789
Tonnesen, S., & Stone, J. 2014, ApJ, 795, 148
Turk, M. J., Smith, B. D., Oishi, J. S., et al. 2011, ApJS, 192, 9
Vijayaraghavan, R., & Ricker, P. M. 2015, MNRAS, 449, 2312
Vijayaraghavan, R., & Ricker, P. M. 2017, ApJ, submitted (arXiv:1702.06138)
Vikhlinin, A., Markevitch, M., Forman, W., & Jones, C. 2001, ApJL, 555, L87
Villalobos, Á, De Lucia, G., Borgani, S., & Murante, G. 2012, MNRAS, 424, 2401
Villalobos, Á, De Lucia, G., & Murante, G. 2014, MNRAS, 444, 313
Voigt, L. M., & Fabian, A. C. 2004, MNRAS, 347, 1130
Voit, G. M. 2011, ApJ, 740, 28
Vollmer, B., Cayatte, V., Balkowski, C., & Duschl, W. J. 2001, ApJ, 561, 708
Wagh, B., Sharma, P., & McCourt, M. 2014, MNRAS, 439, 2822
Weinmann, S. M., van den Bosch, F. C., Yang, X., & Mo, H. J. 2006, MNRAS, 366, 2
Yamasaki, N. Y., Ohashi, T., & Furusho, T. 2002, ApJ, 578, 833
Zabludoff, A. I., & Mulchaey, J. S. 1998, ApJ, 496, 39
Zakamska, N. L., & Narayan, R. 2003, ApJ, 582, 162
Zhang, B., Sun, M., Ji, L., et al. 2013, ApJ, 777, 122